

Simulations of divertor designs that spatially separate power and particle exhaust using mid-leg divertor particle pumping

J.H. Yu^{a,*}, R.S. Wilcox^b, R. Maurizio^a, A. Holm^c, S.L. Allen^c, W. Choi^a, M.E. Fenstermacher^c, M. Groth^d, A.W. Leonard^a, A.G. McLean^c, F. Scotti^c, M.W. Shafer^b

^a General Atomics, San Diego, 92186 CA, USA

^b Oak Ridge National Laboratory, Oak Ridge, 37831 TN, USA

^c Lawrence Livermore National Laboratory, Livermore, 94550 CA, USA

^d Aalto University, Espoo, Finland

ARTICLE INFO

Keywords:

DIII-D
Divertor design
SOLPS-ITER
Tokamak
Mid-leg pumping
SOL power dissipation

ABSTRACT

Predictive design modeling of a Dissipation-Focused Divertor for future operation in DIII-D reveals that increasing the poloidal distance of the pump duct entrance from the target surface along the low-field side divertor baffle increases neutral compression and modifies the spatial distribution of power dissipation. With a divertor pump located mid-leg between the target and the X-point, SOLPS-ITER boundary plasma simulations without drifts predict the formation of a dense neutral cloud near the target with $> 30\text{x}$ higher neutral compression in detachment, a more stable detachment front located further from the target, and $\sim 25\%$ lower outer midplane separatrix density required for detachment onset, compared to a pump located in the scrape-off layer at the target surface. Up to 19 MW of power flowing into the divertors is modeled using the following two numerical implementations for particle pumping: a specified fraction of particles incident on variable wall sections of the plasma grid is removed from the computational domain (so-called albedo pumping), and a pump duct is modeled which includes dynamics of kinetic neutrals in the duct. The simulations show that the detachment front is located between the divertor target and the X-point and is relatively stable near the pump entrance, without a strong dependence on gas puff rate or injected power. The mid-leg pump design spatially separates the two primary functions of a divertor (power handling and particle exhaust), with the majority of power dissipation occurring near the target plate and particle exhaust taking place further upstream. The benefit of enhanced dissipation using mid-leg pumping comes at the cost of a higher outer midplane separatrix density for a given amount of particle injection.

1. Introduction

Power and particle exhaust remain massive challenges for a fusion pilot plant (FPP) [1,2]. Divertor detachment is the primary approach being considered for mitigating power loads to avoid material erosion and thermal damage such as recrystallization, melting, and cracking. However, achieving and maintaining detachment comes with its own set of challenges, including predicting the power and upstream density required to create a detached divertor [3], control of the detachment front (where electron temperature, T_e , drops to the range of the peak in radiative cooling curves for a given impurity species), and compatibility of detachment with high core plasma confinement.

To address these issues, a modular divertor program has been

initiated at DIII-D to design, install, and test new divertors on a rapid timescale [4]. Here we report on SOLPS-ITER [5] simulations used to design the second divertor in this series known as the Stage 2 Dissipation-Focused Divertor (DFD), which is planned to deepen our understanding of the physics governing power dissipation in H-mode. The goals of the DFD project are to achieve a stable detachment front between the target and the X-point, and to test and ultimately improve boundary plasma models to reduce uncertainties in predictive modeling for an FPP.

Modeling and experiments have been previously carried out to investigate various divertor designs, including the effects of divertor shaping and baffling [6–18], divertor depth [4,19], and particle pump location [20]. In Sang's work [20], the emphasis was on achieving

* Corresponding author.

E-mail address: yujh@fusion.gat.com (J.H. Yu).

detachment at the lowest possible upstream density and determining how the pump exhaust rate depends on the pump location. In the present work, we demonstrate that a mid-leg divertor pump enables neutral particles to accumulate near the target plate, which enhances dissipation and favorably affects the location and stability of the detachment front in the divertor.

Much of previous boundary modeling has shown that tension exists between the two fundamental purposes of a divertor: 1) power dissipation, which relies on a sufficiently dense neutral population in order to exploit plasma-neutral interactions, and 2) particle removal via pumping, which is necessary for density control and to prevent helium ash from diluting a burning plasma. This tension exists because particle pumping removes particles from the divertor that are essential for power dissipation.

Here, simulation results are presented for divertor designs with a mid-leg pump, which aim to resolve this tension by spatially separating power dissipation and particle removal, with dissipation occurring in a region of high particle density near the target, and particles removed through a pump duct located upstream of the target. The modeled pump location is varied as a function of the distance from the divertor target plate on the common flux side of the outer divertor baffle. Results from a model with an expanded computational domain that includes modeling of kinetic neutrals in the pump duct at a fixed upstream location are then shown. Additional design elements of the DFD include a deep baffled divertor structure with sufficient volume to dissipate heat flux expected in higher power scenarios enabled by DIII-D upgrades aiming to achieve regimes closer to an FPP. Simulations with these parameters predict that

mid-leg pumping results in a higher level of dissipation than a conventional pump located at the divertor target plate, and an increased stability of the detachment front. The trade-off is higher upstream density for a given particle throughput; however, the required upstream density is decreased for a given level of detachment, and therefore the pumping throughput requirement is reduced from the perspective of divertor performance.

2. Modeling setup

Modeling is performed using the SOLPS-ITER code package [5] (version 3.0.8), which couples the 2D multi-fluid plasma transport code B2.5 [21] and the 3D kinetic neutral transport code EIRENE [22]. B2.5 provides the plasma background to EIRENE, which uses a Monte Carlo approach to compute the source and sink terms for plasma particles, momentum, and energy due to plasma-neutral collisions. These source and sink terms are then returned to B2.5, and the cycle continues until a steady state solution is reached. Modeling is carried out for a deuterium plasma with carbon wall and divertor targets, which are eroded by physical sputtering (using the modified Roth–Bohdansky formula [23]) and 2% chemical sputtering ($Y_{\text{chem}} = 0.02$). Neutral-neutral collisions are included, $E \times B$ particle drifts are not activated, and the grid resolution is 66 poloidal and 32 radial cells. Core boundary conditions of the computational domain are specified using a deuterium injection rate of $1.7 \times 10^{21} \text{ s}^{-1}$ to simulate realistic fueling from DIII-D neutral beam injection (NBI) of 16 MW, and injected power ranging from 4 to 25 MW split equally between electrons and ions. Gas puffing is implemented

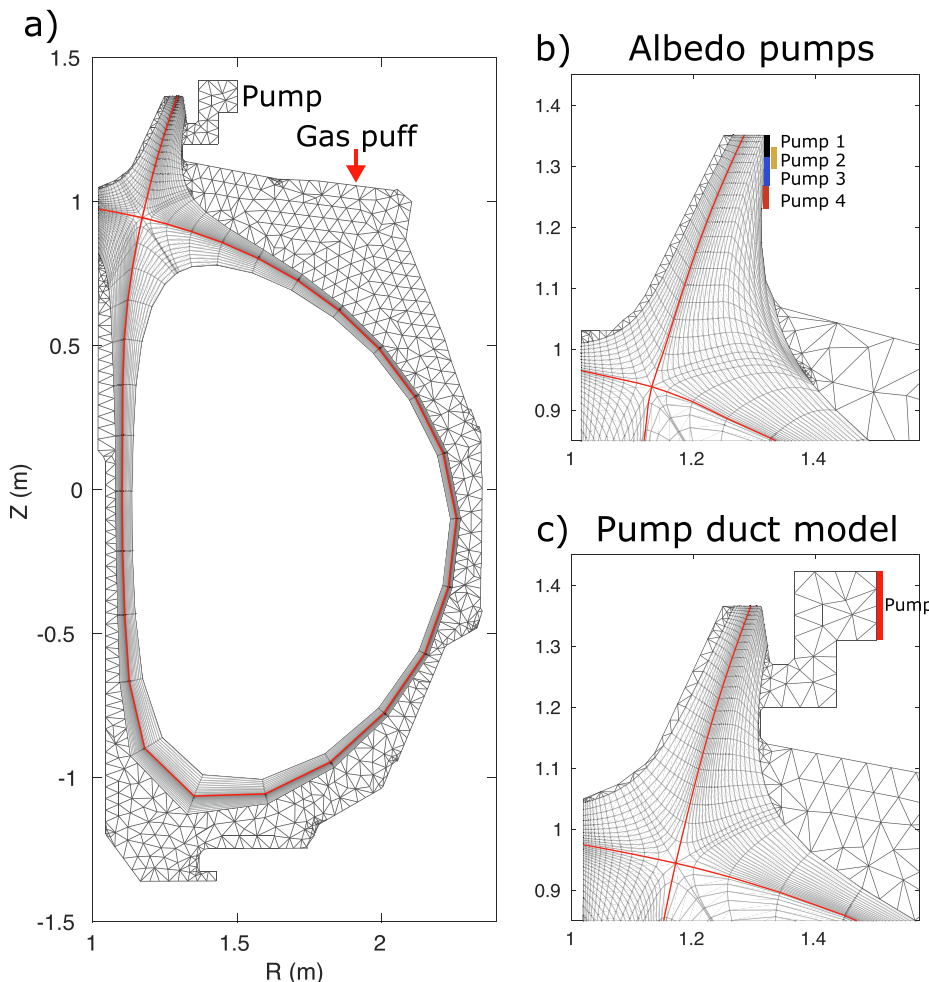


Fig. 1. SOLPS-ITER computational domain for a mid-leg pump duct model is shown in a) and c) and discussed in Section 4. Albedo pumping is implemented in the outer divertor at four locations shown in b) and discussed in Section 3.

from a section of the upper outer main chamber wall (Fig. 1a) to vary the density with puff rates ranging from 0 to $3 \times 10^{22} \text{ s}^{-1}$ (849 torr-L/s). Cross-field diffusive transport coefficients for particles (D_{\perp}), electron heat (χ_e), and ion heat (χ_i), are user-defined in SOLPS-ITER and set here in a step-wise manner to create a transport barrier at the pedestal, and increased in the scrape-off-layer (SOL) to crudely approximate intermittent transport. Transport coefficients are chosen based on the following constraints from previous experimental data and scalings: $n_{e,\text{sep}}/n_{e,\text{ped}}$ between 0.5 and 0.6 [24], particle density at the inner boundary of the computational domain less than the Greenwald density, and the scrape-off layer heat flux width guided by the Eich scaling [25]. In the core, separatrix, and far-SOL regions, $D_{\perp} = 0.5, 0.1$, and $2.0 \text{ m}^2/\text{s}$, and $\chi_e = \chi_i = 1.0, 0.5$, and $10 \text{ m}^2/\text{s}$, respectively, while in the divertor and private flux regions, spatially constant transport coefficients of $D_{\perp} = 2.5 \text{ m}^2/\text{s}$ and $\chi_e = \chi_i = 5.0 \text{ m}^2/\text{s}$ are used. The recycling coefficient on plasma-facing surfaces is set to unity everywhere except on the surface representative of the location of a liquid helium cryogenic pump in the model. Standard Bohm sheath boundary conditions [16] are applied at the targets. Two numerical schemes are implemented for particle pumping (Fig. 1), which are described in the following two sections.

3. Pump location scan using albedo pumping

The first type of pumping implementation is used to investigate the effects of pump location on the divertor state, and utilizes so-called albedo pumping, or surface pumping, directly on a section of the B2.5 grid at the vessel wall (Fig. 1b). Albedo pumping (instead of more accurate modeling of neutrals in the pump duct) is required for the version of SOLPS-ITER used here when the plasma intersects the pump entrance (or surface), and has been used elsewhere [20]. The recycling coefficient R is specified to be < 1 on the albedo surface which removes a fraction $(1-R)$ of all particles incident on the surface, with the chosen value of R based on the experimentally measured pumping speed in DIII-D of $\sim 40 \text{ m}^3/\text{s}$ [26]. The effective pumping speed S is related to the particle removal fraction (i.e., surface absorption) as follows: $S = A(1-R)v_{\text{avg}}/4$ [27,28], where A is the surface area of the wall section used for pumping, and v_{avg} is the average velocity of neutral particles incident on the pumping surface, which we assume to be the thermal velocity of D_2 molecules at 300 K, or 1256 m/s. Grid cell sizes (and thus pump surface areas) are not constant throughout the simulation domain, so to keep the same effective pumping speed, the recycling coefficients are chosen to keep $A(1-R)$ constant for all pump locations. For pump 1 located at the

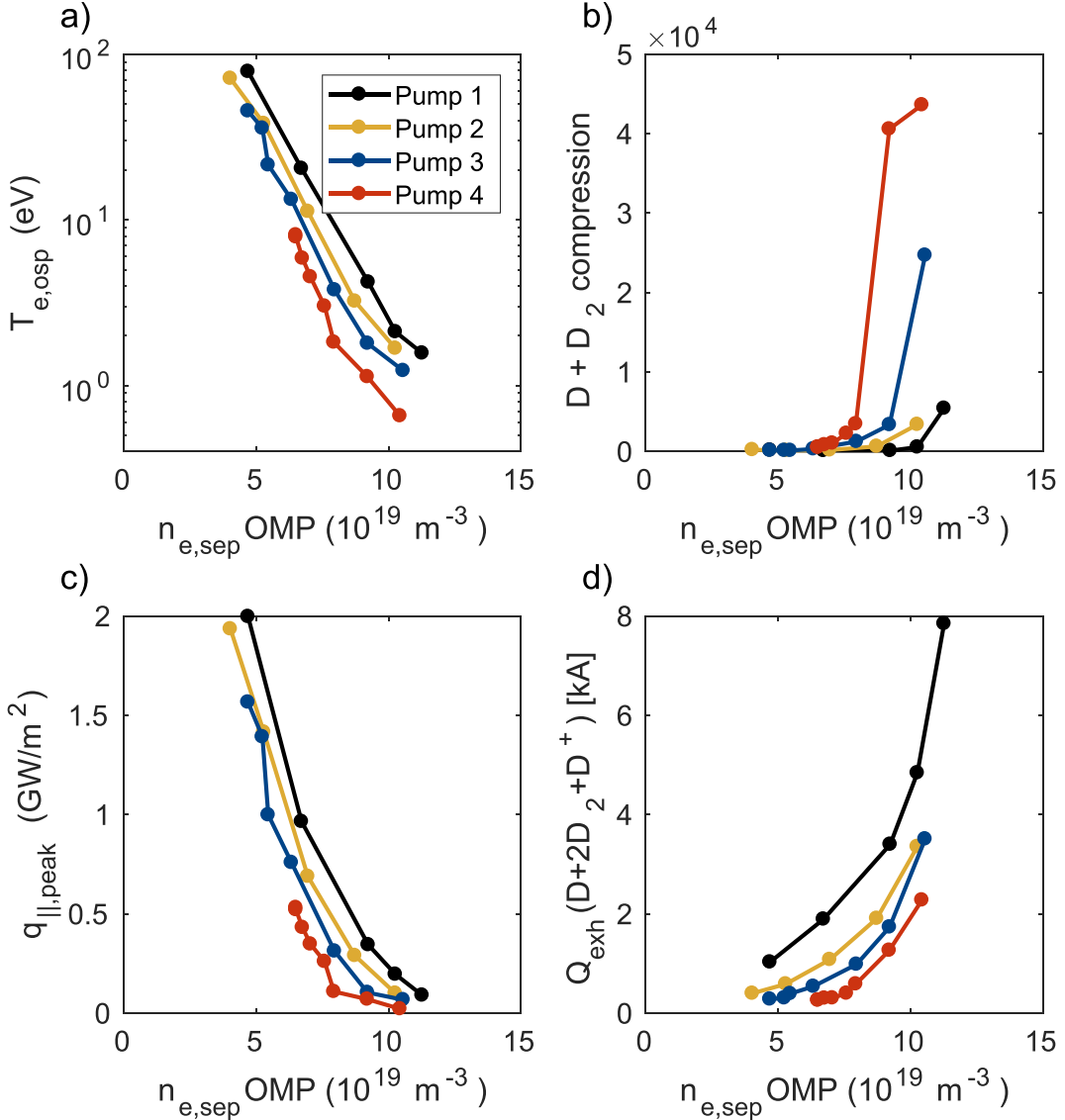


Fig. 2. Outer divertor quantities as a function of outer midplane (OMP) density for four albedo pump locations shown in Fig. 1. a) T_e at the outer strike point, b) neutral deuterium compression in the outer divertor (see text for definition), c) peak parallel heat flux along the outer target, and d) particle removal rate.

target, R is set to 0.7, while for mid-leg albedo pumps, R = 0.684, 0.766, 0.718 at pump locations 2, 3, and 4, respectively (Fig. 1b). Note that while the effective pumping speed was kept the same for all the pump locations, the particle throughput varies as it is determined by the product of the pumping speed and the neutral particle pressure at the pumping surface. The plasma equilibrium used for albedo pumping is from DIII-D upper single null plasma shot 179715, but shifted down to increase the outer leg length, and has $B_T = 2.0$ T, $I_p = 1.28$ MA, $q_{95} = 4.8$, inner divertor leg length = 13.2 cm, and outer divertor leg length = 44.2 cm. Input power to the computational domain is 25 MW, and for the range of gas puff rates and pump locations used here, power flowing into the divertors (calculated at the entrance to the divertors at the X-point) ranges from 15.5 to 19.3 MW.

Varying the albedo pump location reveals a significant effect on neutral dynamics and dissipation in the outer divertor. Dissipation increases monotonically with upstream density, as expected. Importantly, the simulation results also reveal that for a given upstream density, dissipation increases as the pump is moved further poloidally from the target, due to a local high neutral pressure region at the target from recycled neutrals as seen in Fig. 2a–c. The increase in neutral compression with a mid-leg pump compared to a target pump is significant, and is a key feature of the DFD design. Here, neutral compression is defined as the average of the combined atomic and molecular neutral deuterium density along the target divided by the average upstream neutral deuterium density along a radial profile from the X-point to the outer edge of the grid. In addition, Fig. 2a shows the outer strike point T_e in the case using mid-leg pumping drops below 10 eV (taken to be the onset of detachment) at approximately 25% lower outer midplane separatrix density (extrapolated) compared to the target pump case.

In the mid-leg pump simulations, particle throughput is lower compared to that of a pump located at the target for a given upstream density. This is seen in Fig. 2d, and is due to the decreased solid angle of acceptance of a mid-leg pump for particles recycled at the target plate. In addition, for a pump located beyond the ionization mean free path from the target, the dynamics of particles entering the pump can no longer be considered ballistic trajectories from the target plate. The particle throughput at the pump surface matches the particle injection rate into the simulation, regardless of where the pump is located, due to the particle flux boundary condition at the core and no wall absorption. As the pump is moved further upstream from the divertor target, the fraction of particle throughput that consists of fast reflected particles sourced at the divertor target decreases while the fraction due to thermalized molecular deuterium increases. For pump location 4, the density cannot be decreased further than what is shown in Fig. 2 unless the core boundary condition is altered.

Radial profiles of outer midplane and outer target quantities are shown in Fig. 3 for the target pump (black, using the '1' location in Fig. 1b) and a mid-leg pump (green and red, using the '4' location in Fig. 1b), with roughly similar powers entering the divertors (17.4, 18.3, and 17.5 MW for the black, green, and red cases, respectively). Profiles are shown for the two pump locations with matched outer midplane profiles, as seen by comparing the black and red lines, and for approximately matched downstream profiles, as seen by comparing the black and green lines. Fig. 3a–b show the matched outer midplane plasma profiles are essentially identical despite using different gas puff rates of $2.0 \times 10^{22} \text{ s}^{-1}$ and $0.5 \times 10^{22} \text{ s}^{-1}$ for target pump 1 and mid-leg pump 4, respectively. For these matched outer midplane cases, the outer midplane $n_{e,\text{sep}} = 9.2 \times 10^{19} \text{ m}^{-3}$ and $T_{e,\text{sep}} \sim 210$ eV. The fact that main chamber profiles match at different gas puff rates is due to the higher

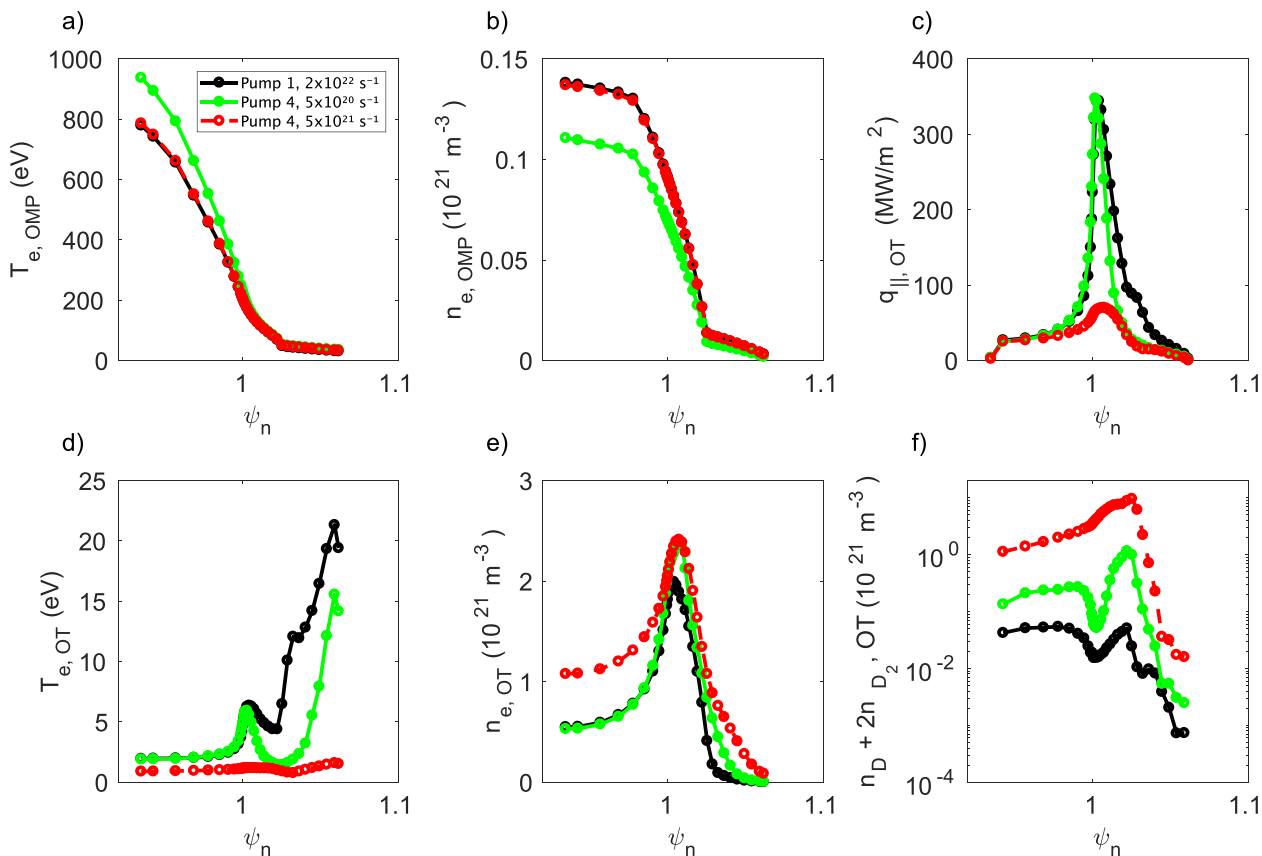


Fig. 3. Radial profiles for pumping at the target (black) and mid-leg pumping (green and red). Black and red are matched upstream, and black and green are approximately matched downstream. Profiles at the outer midplane show a) T_e and b) n_e ; and at the outer target (OT) c) $q_{||}$, d) T_e , e) n_e , and f) neutral deuterium density.

throughput that can be maintained by pump 1 compared to pump 4 for a given upstream density.

The benefit of the mid-leg pump compared to the target pump in terms of dissipation is evident by comparing the matched outer mid-plane profiles (black and red) in Fig. 3c-e, showing lower $q_{||}$, lower T_e , and higher n_e , across the entire target. In detached conditions, the mid-leg pump (red curves) has a moderately larger $n_{e,osp}$ (by 14%) and a much higher neutral density at the outer strike point (170x) compared to the target pump (Fig. 3f). Even with high upstream density shown here, the target pump case is not fully detached (Fig. 3d), because the pump removes the particles needed for dissipation. This is seen in Fig. 3f where the black line from the target pump simulation shows only a small level of accumulation of recycled neutrals.

In addition, by comparing approximately matched downstream profiles (black and green in Fig. 3) for the two pump locations, the difference in outer midplane profiles required to produce similar peak heat fluxes at the outer target can be seen, with the outer midplane separatrix density and temperature of the mid-leg pump case relative to the target pump case being 77% and 119%, respectively. Neutral density at the outer strike point in the mid-leg pump case is 4.8x larger than that in the target pump even though the gas puff rate for the target pump case is 40x larger than that for the mid-leg pump case (puff rates of $5 \times 10^{20} \text{ s}^{-1}$ and $2 \times 10^{22} \text{ s}^{-1}$ for the mid-leg and target pumps, respectively). This divertor density is not sufficient to completely detach the outer divertor as seen in the green curve of Fig. 3d, although the outer corner of the divertor reaches a low T_e value of 1.4 eV.

The 2D profiles of T_e and n_e provide additional information to determine effects from mid-leg pumping compared to a conventional pump located at the target. Fig. 4 shows a high density, cold region develops near the target in the mid-leg pump divertor (right column), with a spatial distribution that extends further from the target compared to conventional pumping at the target (left column). The two simulations here have the same upstream profiles and are the black and red cases used in Fig. 3. The cold ($< 10 \text{ eV}$) plasma region in the mid-leg pump divertor (Fig. 4b) shows the detachment front is located off the divertor target, and extends poloidally upstream along the outer baffle. A high electron density region near the outer corner of the divertor is evident in Fig. 4d, which is in stark contrast to the case with the pump located at the target (Fig. 4c). In the next section we move beyond albedo pumping and show results from a more complete model of mid-leg pumping that includes kinetic neutrals in the pump duct.

4. Model of mid-leg pump duct with kinetic neutrals

In the second type of pumping implementation, the model domain contains the pump duct so that kinetic neutral dynamics in the pump duct can be accounted for. In this model the pump entrance is located 9.4 cm poloidally upstream of the target surface on the SOL side. Particles are removed from the simulation domain when they are incident on an absorbing EIRENE surface located at the back end of the pump duct to be representative of a liquid helium cryopump, as shown in Fig. 1c. The surface absorption, α , at the back of the pump duct structure

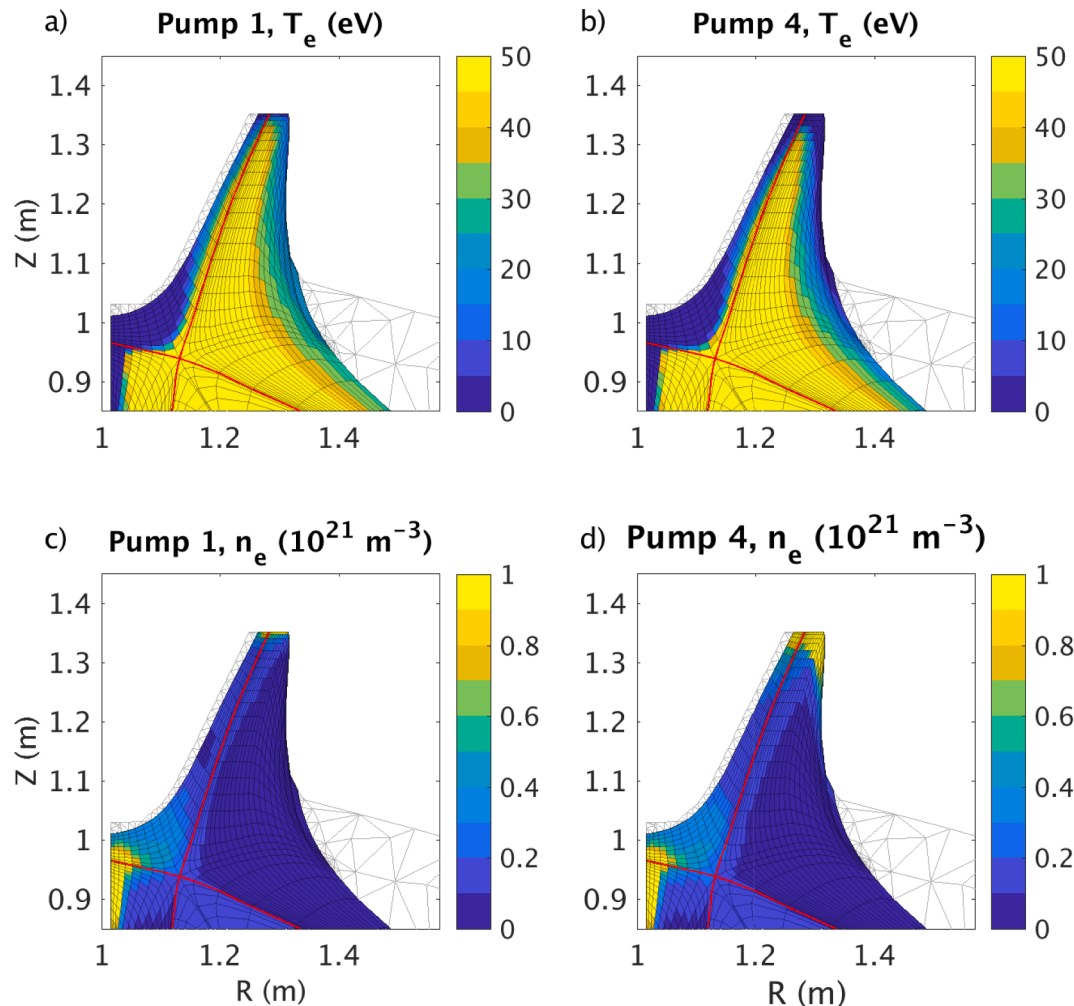


Fig. 4. The target pump at location 1 (left column) compared to the mid-leg pump at location 4 (right column) for T_e a) – b) and n_e c) – d), for the same upstream conditions.

as shown in Fig. 1c is set to 0.12 to match the experimentally measured DIII-D pumping speed [26] using the expression shown in Section 3, with $\alpha = 1-R$. This pump duct model offers higher fidelity than albedo pumping by allowing kinetic neutrals to thermalize on duct walls, improving the accuracy of the thermal velocity assumption for particles incident on the absorbing surface. The plasma equilibrium used here (simulated discharge 981809 at 2400 ms) is computed by TokSys [29] which is a time-dependent Grad-Shafranov solver that incorporates DIII-D coil current limits and response times, and has $B_T = 2.1$ T, $I_p = 1.8$ MA, $q_{95} = 3.3$, inner divertor leg length = 17.3 cm, and outer divertor leg

length = 44.4 cm. The mid-leg pump duct model has a slightly smaller radial extent of the grid (maximum normalized poloidal flux coordinate $\psi_n = 1.061$) compared to the albedo pump cases in Section 3 (maximum $\psi_n = 1.045$), due to limitations of non-extended grid versions of SOLPS-ITER.

Input power to the grid ranges from 4 to 25 MW, with power flowing into the divertors ranging from 2.7 to 17.1 MW due to approximately 30% of the power escaping radially off the grid (a small fraction of injected power is radiated before entering the divertors). These radial losses occur despite the radial extent of the SOL grid (13.1 mm) at the

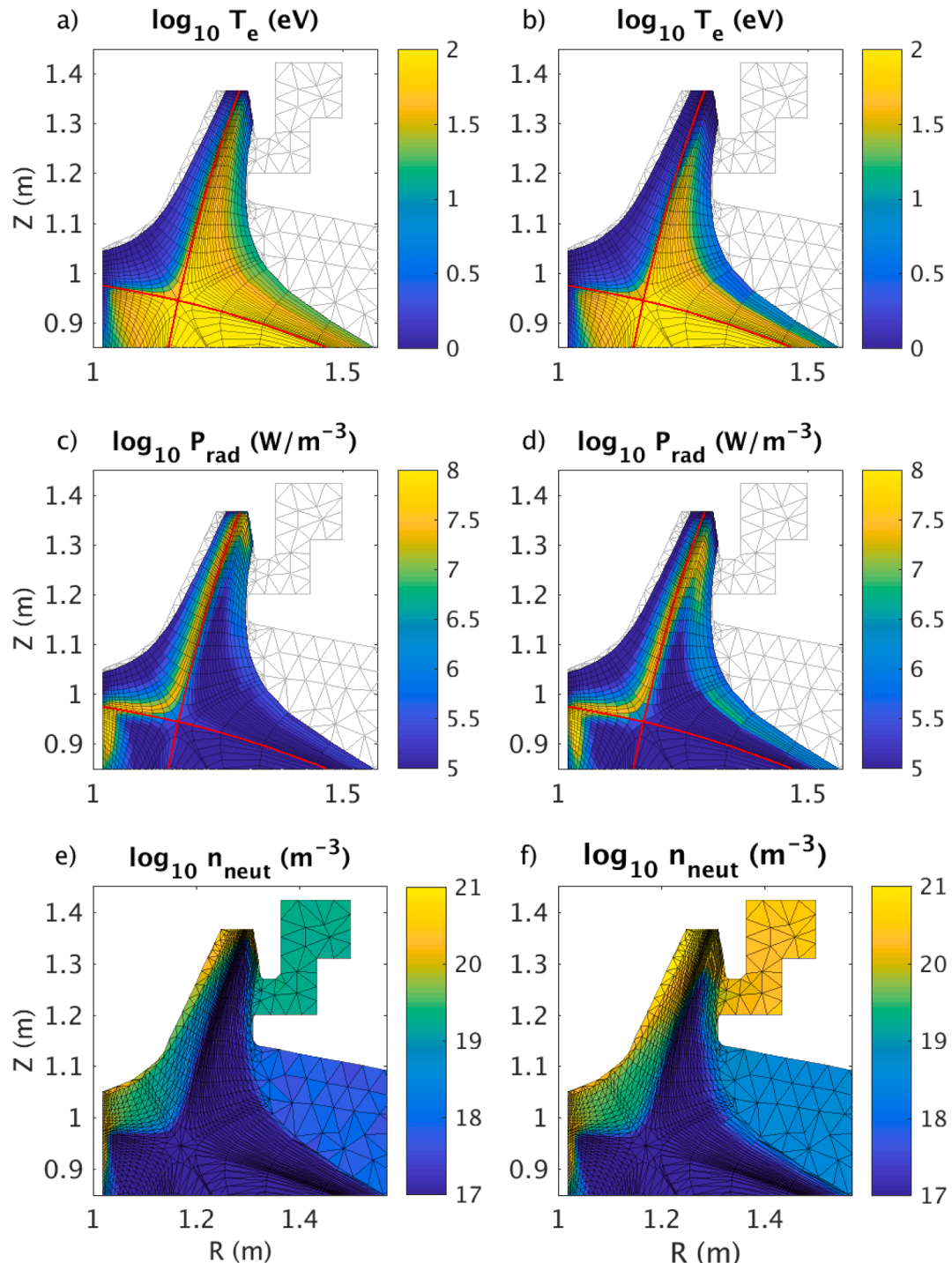


Fig. 5. Simulations of a mid-leg particle pump for no gas puffing (left column) with 8.5 MW into the divertors, and D_2 gas puff rate of $3.0 \times 10^{22} \text{ s}^{-1}$ (right column) with 8.0 MW into the divertors. a)-b) T_e , c)-d) total radiated power density, e)-f) neutral deuterium density ($n_D + 2n_{D_2}$).

outer midplane being approximately 7x the heat flux width (1.7–2.1 mm) in the simulations. Previous modeling using matched upstream and divertor plasma profiles to experimental profiles showed radial power losses up to 72% [9] and 90% [30], suggesting that purely diffusive cross-field transport coefficients may not capture far-SOL transport physics, although more work is necessary to resolve this issue. Radial particle escape also occurs, with the radial particle flux at the outer boundary of the grid ranging from 12% to 36% of the poloidal particle flux to the divertor targets (higher radial boundary flux occurs for higher gas puff rates). The outer midplane electron density profile decays towards the edge of the grid and is not truncated, with a density decay length of approximately 6 mm or $\sim 1/2$ the SOL grid width.

Radial power and particle losses at the edge of the plasma grid in SOLPS-ITER impact simulation accuracy. For radial power losses, any heat flux that reaches the radial boundary simply disappears from the simulation domain, effectively reducing the power entering the divertors. To account for this we state not only the power injected into the grid, but also the actual power flowing into the divertors. Ions that reach the radial boundary of the plasma grid are artificially converted to neutrals, which can lead to inaccurate neutral transport and the simulated recycling and ionization occurring in physically incorrect locations [31–33]. Despite the limitations due to power and particles escaping the simulation domain, the physics of atomic processes leading to dissipation within the divertors is modeled using a broad range of EIRENE reactions [9]. For the present study, power flowing into the divertors is more relevant than power flowing radially through the core, SOL, and grid edge, as our primary focus is on dissipation and the detachment front in the divertor.

The simulations reveal strong dissipation and a stable detachment front across a range of gas puff injection rates and input powers. In Fig. 5, results using zero puffing are shown in the left column, and using a gas puff rate of $3.0 \times 10^{22} \text{ s}^{-1}$ in the right column. In both cases a cold region develops along the target, and with gas puffing, the cold region extends away from the target as seen in Fig. 5b. Without puffing, the spatial distribution of radiated power in the outer divertor SOL is localized near the target (Fig. 5c), while in the higher density case with gas puffing, the radiation is localized near the pump duct entrance as seen in Fig. 5d. Carbon radiation dominates over deuterium radiation, accounting for 86% and 81% of the total radiation in the divertors with no gas puffing and with gas puffing, respectively.

When the pump is located poloidally upstream of the divertor target, most of the pumped particles are in the form of thermalized molecular D₂ rather than fast reflected atoms from the target plate. The total neutral deuterium density ($n_D + 2n_{D_2}$) in the pump duct increases by an order of magnitude in the $3.0 \times 10^{22} \text{ s}^{-1}$ gas puff case compared to no gas puff (Fig. 5e, f), which is a trivial (but informative) result since the no gas puff case only has deuterium injected from the core with a flux boundary condition of $1.7 \times 10^{21} \text{ s}^{-1}$.

A primary goal of the DFD is to achieve a stable detachment front between the target and the X-point. We define $T_e = 10 \text{ eV}$ as the onset of power detachment as momentum loss begins to increase significantly as T_e drops below this value [34]. Fig. 6a and 6b show the dependency of the vertical location of the $T_e = 2, 5, \text{ and } 10 \text{ eV}$ fronts along the outer leg separatrix on the gas puff rate and power flowing into the divertors. The divertor state and detachment front location evolve with gas puff rate, starting from a moderately detached state even without gas puffing. For

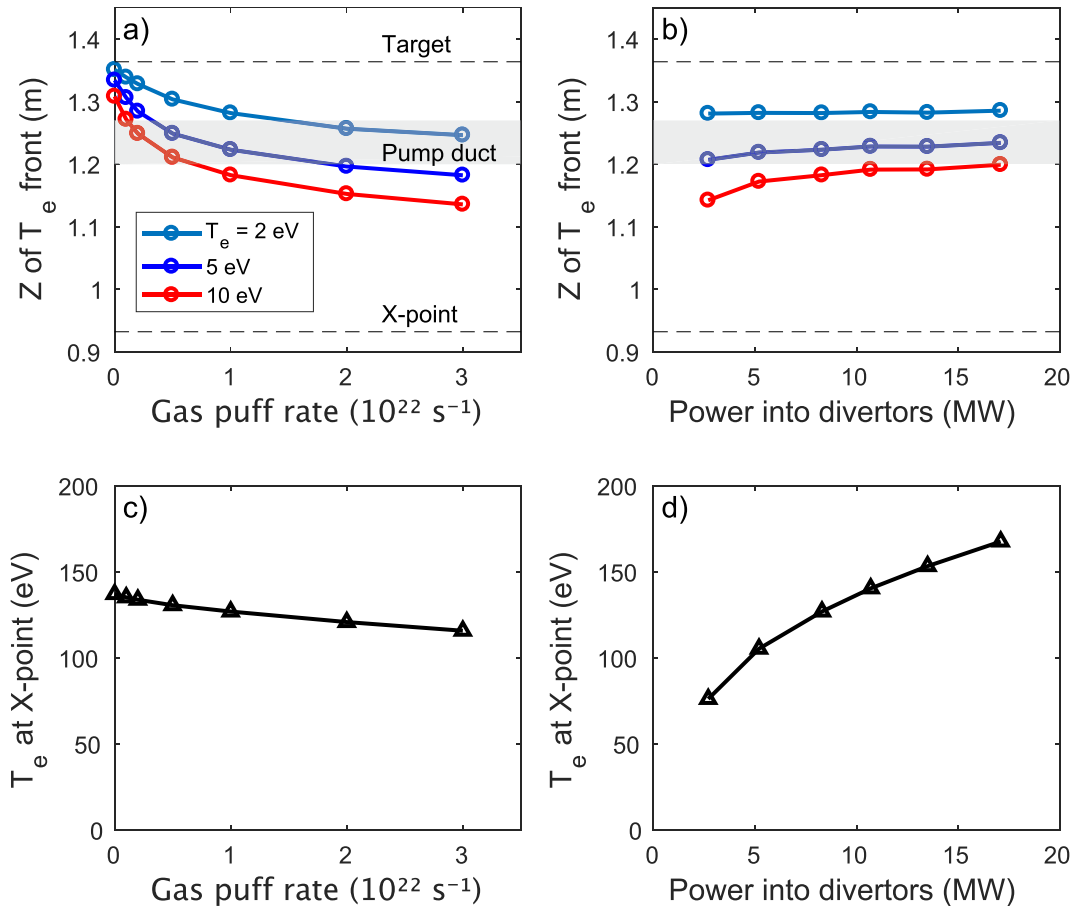


Fig. 6. Simulations with mid-leg pumping including kinetic neutrals in the pump duct. a) – b) Vertical locations of $T_e = 2, 5, \text{ and } 10 \text{ eV}$ contours along the outer leg separatrix, and c) – d) T_e at the X-point. Left column is a gas puff scan at fixed input power, with power into the divertors ranging from 8.0 to 8.5 MW. Right column is a power scan at fixed gas puff rate of $1 \times 10^{22} \text{ s}^{-1}$. Outer divertor target and X-point vertical locations are marked with dashed lines in a) – b), and shaded regions show vertical location of the pump duct entrance.

the gas puff scan shown here, the input power to the domain is fixed at 12.5 MW, and power flowing into the divertors decreases from 8.5 to 8.0 MW as gas puffing is increased, due to increased power radiated in the SOL and increased power lost from the grid as a result of profile changes.

As the gas puff is increased, the detachment front moves away from the target and maintains a relatively stable vertical location near the mid-leg pump duct entrance, as seen in Fig. 6a. As the gas puff rate is further increased up to $3 \times 10^{22} \text{ s}^{-1}$ ($n_{e,\text{sep},\text{omp}} = 9.8 \times 10^{19} \text{ m}^{-3}$), the $T_e = 10 \text{ eV}$ front moves only a modest distance poloidally upstream of the pump duct entrance, and importantly for core plasma confinement and performance, does not approach the X-point for the range of parameters scanned here. T_e at the X-point decreases throughout the gas puff scan, but remains above 100 eV even at the highest puff rate as shown in Fig. 6c.

At fixed gas puff of $1.0 \times 10^{22} \text{ s}^{-1}$, the power scan in Fig. 6b shows remarkable stability of the detachment front location over the range of parameters used here. At low power of 2.7 MW flowing into the divertors, the detachment front is located near the upstream edge of the pump duct entrance. As power is increased, the detachment front moves slightly closer to the target but never reaches it, and stays in a region near the pump duct entrance. T_e at the X-point increases with power as seen in Fig. 6d.

5. Discussion and conclusions

The conclusions from SOLPS-ITER simulations presented here, as well as an extensive set of complementary fluid plasma and neutral simulations using UEDGE [35], appear robust, despite uncertainties regarding details of ad-hoc cross-field transport coefficients. A divertor design with a mid-leg pump spatially decouples the two primary roles of a divertor, namely power and particle exhaust. By removing particles slightly poloidally upstream of the divertor target plate, power dissipation is enhanced due to neutral accumulation at the target, allowing the formation of a neutral cushion that radiates power isotropically. A mid-leg pump acts similar to a relief valve; i.e., the mid-leg pressure buildup from neutrals generated at the divertor target or from volumetric recombination is limited because neutrals can transport into the pump duct, resulting in a relatively stable position of the 10 eV front during detachment as shown by the asymptotic behavior in Fig. 6a. This provides a viable pathway for integrating a dissipative divertor solution with a high-performance core plasma. Particle pumping is less efficient for a mid-leg pump compared to a target pump in the sense that the core density is greater for a given gas puff rate, but the core density required for a given degree of detachment is reduced due to more effective trapping of neutrals deep in the divertor. Compared to albedo pumping, the pump duct model provides more complete neutral particle physics and a better approximation to the previously measured pumping speed in DIII-D [26] due to thermalized deuterium molecules in the pump duct.

The SOLPS-ITER simulations predict detachment front stability with a mid-leg pump, however, no drifts are included here. In complementary UEDGE simulations [35] with cross-field particle drift effects included, the particle drift direction is found to affect the pumping rate which in turn influences the divertor plasma conditions and detachment front location. With favorable ion $\mathbf{B} \times \nabla B$ drift direction (into the divertor), the radial $\mathbf{E} \times \mathbf{B}$ drifts in the divertor are directed across the separatrix into the private flux region and thus the neutral pressure in the common flux side of the divertor and the effect of the pump are reduced, leading to reduced detachment front stability. In the unfavorable ion $\mathbf{B} \times \nabla B$ drift direction, $\mathbf{E} \times \mathbf{B}$ drifts direct particles toward the outer baffle where the pump is located, and the detachment front stability is increased for the range of gas puff rates that were achievable in the simulations.

Future work includes turning on drifts in SOLPS-ITER for higher fidelity modeling, and exploring strategies to simultaneously match experimental plasma profiles while minimizing power lost radially off

the domain of the grid. Once the DFD is installed, boundary codes will be used to interpret experimental results, and DFD data will be used to challenge and validate boundary models for better predictive capability for an FPP.

Disclaimer

This report was prepared as an account of work sponsored by an agency of the United States Government. Neither the United States Government nor any agency thereof, nor any of their employees, makes any warranty, express or implied, or assumes any legal liability or responsibility for the accuracy, completeness, or usefulness of any information, apparatus, product, or process disclosed, or represents that its use would not infringe privately owned rights. Reference herein to any specific commercial product, process, or service by trade name, trademark, manufacturer, or otherwise does not necessarily constitute or imply its endorsement, recommendation, or favoring by the United States Government or any agency thereof. The views and opinions of authors expressed herein do not necessarily state or reflect those of the United States Government or any agency thereof.

CRediT authorship contribution statement

J.H. Yu: Writing – original draft, Writing – review & editing, Visualization, Validation, Software, Investigation, Formal analysis, Data curation, Conceptualization. **R. Wilcox:** Writing – review & editing, Investigation, Conceptualization. **R. Maurizio:** Investigation. **A. Holm:** Investigation. **S.L. Allen:** Validation. **W. Choi:** Investigation. **M.E. Fenstermacher:** Validation. **M. Groth:** Validation. **A.W. Leonard:** Validation. **A.G. McLean:** Validation. **F. Scotti:** Validation. **M.W. Shafer:** Validation, Conceptualization.

Declaration of competing interest

The authors declare that they have no known competing financial interests or personal relationships that could have appeared to influence the work reported in this paper.

Acknowledgments

The authors would like to thank the entire DIII-D Stage 2 Divertor working group for their constructive discussions. This material is based upon work supported by the U.S. Department of Energy, Office of Science, Office of Fusion Energy Sciences, using the DIII-D National Fusion Facility, a DOE Office of Science user facility, under Awards DE-FC02-04ER54698, DE-AC05-00OR22725, and DE-AC52-07NA27344.

Data availability

Data will be made available on request.

References

- [1] H. Zohm, et al., On the physics guidelines for a tokamak DEMO, Nucl. Fusion 53 (2013) 073019, <https://doi.org/10.1088/0029-5515/53/7/073019>.
- [2] A.Q. Kuang, et al., Conceptual design study for heat exhaust management in the ARC fusion pilot plant, Fus. Eng. Design 137 (2018) 221–242, <https://doi.org/10.1016/j.fusengdes.2018.09.007>.
- [3] M. Wischmeier, et al., Current understanding of divertor detachment: Experiments and modelling, J. Nucl. Mat. 390-391 (2009) 250–254, <https://doi.org/10.1016/j.jnucmat.2009.01.081>.
- [4] R. Maurizio, et al., Modeling deep slot divertor concepts at DIII-D using SOLPS-ITER with drifts, Nucl. Mater. Energy 34 (2023) 101356, <https://doi.org/10.1016/j.nme.2022.101356>.
- [5] X. Bonnin, et al., Presentation of the new SOLPS-ITER code package for tokamak plasma edge modelling, Plasma Fusion Res. 11 (2016) 1403102, <https://doi.org/10.1585/pfr.11.1403102>.
- [6] A. Loarte, et al., Effects of divertor geometry on tokamak plasmas, Plasma Phys. Control. Fusion 43 (2001) R183-R224, <https://doi.org/10.1016/j.nme.2019.03.021>.

- [7] H.Y. Guo, et al., First experimental tests of a new small angle slot divertor on DIII-D, Nucl Fusion 59 (2019) 86054, <https://doi.org/10.1088/1741-4326/ab26ee>.
- [8] L. Casali, et al., The effect of neutrals in the new SAS divertor at DIII-D as modelled by SOLPS, Nucl. Mater. Energy 19 (2019) 537–543, <https://doi.org/10.1088/0741-3335/43/6/201>.
- [9] R. Maurizio, et al., Numerical assessment of the new V-shape small-angle slot divertor on DIII-D, Nucl. Fusion 61 (2021) 116042, <https://doi.org/10.1088/1741-4326/ac27c8>.
- [10] X. Ma, et al., First evidence of dominant influence of $E \times B$ drifts on plasma cooling in an advanced slot divertor for tokamak power exhaust, Nucl. Fusion 61 (2021) 54002, <https://doi.org/10.1088/1741-4326/abde75>.
- [11] B. Lipschultz, et al., Divertor physics research on Alcator C-Mod, Fusion Sci. Technol. 51 (2007) 369–389, <https://doi.org/10.13182/FST07-A1428>.
- [12] A.E. Jaervinen, et al., $E \times B$ flux driven detachment bifurcation in the DIII-D tokamak, Phys. Rev. Lett. 121 (2018) 075001, <https://doi.org/10.1103/PhysRevLett.121.075001>.
- [13] M. Wigram, et al., Performance assessment of long-legged tightly-baffled divertor geometries in the ARC reactor concept, Nucl. Fusion 59 (2019) 106052, <https://doi.org/10.1088/1741-4326/ab394f>.
- [14] M.W. Shafer, et al., Dependence of neutral pressure on detachment in the small angle slot divertor at DIII-D, Nucl. Mater. Energy 19 (2019) 487, <https://doi.org/10.1016/j.nme.2019.04.003>.
- [15] A.L. Moser, et al., The effect of divertor closure on detachment onset in DIII-D, Nucl. Mater. Energy 19 (2019) 67, <https://doi.org/10.1016/j.nme.2019.01.017>.
- [16] H. Du, et al., Manipulation of $E \times B$ drifts in a slot divertor with advanced shaping to optimize detachment, Nucl. Fusion 60 (2020) 126030, <https://doi.org/10.1088/1741-4326/abb53f>.
- [17] O. Février, et al., Divertor closure effects on the TCV boundary plasma, Nucl. Mater. Energy 27 (2021) 100977, <https://doi.org/10.1016/j.nme.2021.100977>.
- [18] JET Team (prepared by R.D. Monk), Recent results from divertor and scrape-off layer studies at JET, Nucl. Fusion 39 (1999) 1751. DOI 10.1088/0029-5515/39/11Y/315.
- [19] C. Sang, et al., SOLPS analysis of neutral baffling for the design of a new diverter in DIII-D, Nucl. Fusion 57 (2017) 056043, <https://doi.org/10.1088/1741-4326/aa6548>.
- [20] C. Sang, et al., The role of divertor pumping in plasma detachment and particle exhaust in a closed divertor, Nucl. Fusion 61 (2021) 016022, <https://doi.org/10.1088/1741-4326/abc356>.
- [21] R. Schneider, et al., Plasma edge physics with B2-Eirene, Contrib. Plasma Phys. 46 (2006) 3–191, <https://doi.org/10.1002/ctpp.200610001>.
- [22] D. Reiter, et al., The EIRENE and B2-EIRENE codes, Fusion Sci. Technol. 47 (2005) 172–186, <https://doi.org/10.13182/FST47-172>.
- [23] J. Roth, C. Garcia-Rosales, Analytic description of the chemical erosion of graphite by hydrogen ions, Nucl. Fusion 36 (1996) 1647–1659, <https://doi.org/10.1088/0029-5515/36/12/015>.
- [24] A.W. Leonard, et al., Compatibility of separatrix density scaling for divertor detachment with H-mode pedestal operation in DIII-D, Nucl. Fusion 57 (2017) 086033, <https://doi.org/10.1088/1741-4326/aa778c>.
- [25] T. Eich, et al., Scaling of the tokamak near the scrape-off layer H-mode power width and implications for ITER, Nucl. Fusion 53 (2013) 93031, <https://doi.org/10.1088/0029-5515/53/9/093031>.
- [26] R. Maingi, et al., Neutral pressure dynamics in the upper plenums in the DIII-D tokamak, Nucl. Fus. 44 (2004) 909, <https://doi.org/10.1088/0029-5515/44/8/009>.
- [27] J.D. Lore, et al., Optimization of pumping performance in the EAST upgraded divertor, Plasma Phys. Control. Fusion 61 (2019) 065001, <https://doi.org/10.1088/1361-6587/ab110e>.
- [28] D. Reiter. The EIRENE Code User Manual, 2023. <https://www.eirene.de/Documentation/eirene.pdf>.
- [29] A. Welander, et al., Closed-loop simulation with Grad-Shafranov equilibrium evolution for plasma control system development, Fus. Eng. Design 146 Part B (2019) 2361, <https://doi.org/10.1016/j.fusengdes.2019.03.191>.
- [30] R. Wilcox, et al., Interpretive Modeling Using SOLPS-ITER for Pumping Experiments with a Closed Divertor in DIII-D, in Proc. 29th IAEA Fusion Energy Conf., Ex-D/8 Ex-D/8, Vienna, Austria, 2023.
- [31] J.D. Lore, et al., Modeling non-axisymmetry in the DIII-D small angle slot divertor using EMC3-EIRENE, Nucl. Mat. Energy 17 (2018) 152–157, <https://doi.org/10.1016/j.nme.2018.10.006>.
- [32] S. Wiesen, et al., On the role of finite grid extent in SOLPS-ITER edge plasma simulations for JET H-mode discharges with metallic wall, Nucl. Mat. Energy 17 (2018) 174–181, <https://doi.org/10.1016/j.nme.2018.10.013>.
- [33] W. Dekeyser, et al., Plasma edge simulations including realistic wall geometry with SOLPS-ITER, Nucl. Mat. Energy 27 (2021) 100999, <https://doi.org/10.1016/j.nme.2021.100999>.
- [34] P.C. Stangeby, Basic physical processes and reduced models for plasma detachment, Plasma Phys. Control. Fusion 60 (2018) 44022, <https://doi.org/10.1088/1361-6587/aaacf6>.
- [35] A. Holm, et al., Modeling a divertor with mid-leg pumping for high-power H-mode scenarios in DIII-D considering $E \times B$ drift flows, Nucl. Mat. Energy 41 (2024) 101782, <https://doi.org/10.1016/j.nme.2024.101782>.